

www.acsami.org Research Article

Electron—Hole Excitation Induced Softening in Boron Carbide-Based Superhard Materials

Yi He, Yidi Shen, Bin Tang,* and Qi An*



Cite This: ACS Appl. Mater. Interfaces 2022, 14, 25792-25801



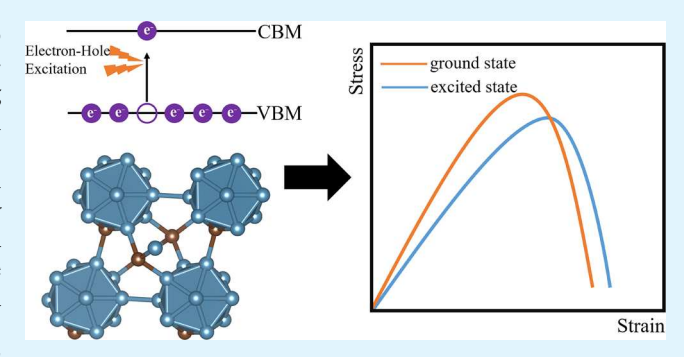
ACCESS I

Metrics & More

Article Recommendations

SI Supporting Information

ABSTRACT: Photomechanical effect in semiconductors refers to a phenomenon that plastic deformation is influenced by light-induced electron—hole (e-h) excitation. To date, increasing amounts of theoretical and experimental studies have been performed to illustrate the physical origin of this phenomenon. In contrast, there has been little discussion about this effect in superhard materials. Here, we adopted constrained density functional theory simulations to assess how e-h excitation influences two boron-based superhard materials: boron carbide (B_4C) and boron subphosphide $(B_{12}P_2)$. We found that the ideal shear strengths of both systems decrease under e-h excited states. Under e-h excitation, the redistribution of electrons and holes



contributes to the decreased strength, weakening the bonds initially broken under the shear deformation. The simulation results provide a fundamental explanation for the softening effects of superhard materials under e-h excitation. This study also provides a basis to tune the mechanical properties of superhard materials via light irradiation.

KEYWORDS: superhard, B₄C, constrained DFT, photomechanical effect, amorphization

1. INTRODUCTION

Electron-hole pairs (EHPs) normally form in semiconductors as the electrons near the valence band maximum are excited to the conduction band through light irradiation with an appropriate wavelength. In turn, these light-induced EHPs will influence the electrical properties of semiconductors used in electronic devices. Additionally, extensive research has established that electron irradiation or light illumination impacts the mechanical properties of many semiconductors, which is known as photomechanical effect.²⁻⁶ For example, the flow stress of CdS in compression increases under light illumination.² Similar phenomena have also been reported in other II-VI compounds. Indeed, Carlsson et al.^{4,5} found that both ZnO and CdTe single crystals display the same lightinduced flow stress increase. However, the physical origin of photomechanical effect remains controversial due to the complex coupling of mechanic loading, electron-hole (e-h) lifetime, and chemical bonding.

Generally, there are two competitive deformation mechanisms in semiconductors, dislocation and deformation twinning. Researchers have conducted in situ transmission electron microscopy (TEM) experiments and found that electron-beam irradiation enhances the dislocation mobility in II–VI ionic semiconductors due to the nonradiative recombination of excited carriers at dislocation cores.^{7,8} It was suggested that the activation energy of dislocation nucleation in semiconductors is less than that under darkness

because the recombination of excited EHPs weakens ionic bonding in ionic semiconductors. A recent experimental study reported that ZnS exhibits different deformation mechanisms under various light illumination conditions. 10 In complete darkness conditions, the ZnS crystal suffers plastic deformation dominated by dislocations at a large strain of 45%. In contrast, under light irradiation conditions, ZnS suffers brittle failure deformation dominated by twinning, implying that the light-irradiated EHPs involve in activating deformation twinning. 10 To explain these interesting findings, Wang et al. performed constrained density functional theory (CDFT) simulations to investigate how excited EHPs in ZnS affect the general stacking fault energy surface (γ -surface). ¹¹ Under lightillumination conditions, ZnS tends to form more twins due to the EHP-weakened ionic bonding. Moreover, EHPs excited by electron beam and photoactivation also have an impact on the mechanical properties of III-V covalent semiconductors. 9,12-16 In our previous study, we combined CDFT simulations, nanoindentation experiments, and TEM measurements to explore this photomechanical effect on III-V

Received: March 29, 2022 Accepted: May 10, 2022 Published: May 24, 2022





semiconductors of GaP, GaAs, and InP. 16 Under light irradiation, excited EHPs weaken covalent bonds, which lowers the energy barrier for the deformation slip and makes these III–V semiconductors more ductile.

It has previously been established that boron carbide and related superhard materials can be considered high-temperature semiconductors because of their excellent thermal stability. For example, boron carbide B_4C is regarded as a p-type semiconductor whose bandgap is 3.84 eV. 17,18 $B_{12}P_2$ is also a semiconductor whose bandgap is 3.35 eV from experimental measurements. 19,20 In addition, early work reported that B_6O is a promising p-type semiconductor with a bandgap of \sim 3.0 eV and high carrier mobility from theoretical calculations. 21 Therefore, it is speculated that the mechanical properties of these superhard materials are affected by light illumination or electron irradiation.

Different from II–VI and III–V semiconductors, dislocation activities and dislocation plasticity are not observed in B₄C and related superhard materials under conventional loading conditions at room temperature due to high lattice resistance. $^{22-24}$ In contrast, B_4C prefers to exhibit abnormal brittle failure under pressure, leading to the formation of amorphization bands. These amorphous bands have been widely observed in B₄C under hypervelocity impact,²⁵ nanoindentation, and scratch experiments.²⁶⁻²⁹ A recent theoretical study has indicated that the formation of amorphization bands can be ascribed to the C-B-C chain reacting with B₁₁C icosahedral clusters under shear deformation, leading to the deconstruction of B₁₁C icosahedra in the crystalline phase.30 Our recent study showed that excess electrons in B₄C are accumulated between the chain and cage, influencing the amorphization of B₄C.³¹ However, the influence of excited EHPs on the amorphization of B₄C remains unknown.

CDFT simulations are performed in this study to explore the effect of e-h excitation on the deformation mechanism of superhard materials B₄C and B₁₂P₂. First, we examined the shear deformation of B₄C along the most plausible slip system of (001)[100] under e-h excitation states. Here, we used the 3index rhombohedral slip system in this article. Our results indicated that e-h excitation lowers the ideal shear strength of $B_{4}C$. This arises from the excited e-h redistribution where the holes are distributed among the B-B bonds between icosahedra, while the excited electrons are distributed among the B₁₁C icosahedra. Then, we examined the shear response of $B_{12}P_2$ along three plausible slip systems: $(011)[2\overline{11}]$, (111) $[1\overline{10}]$, and (001)[100] under light illumination. $B_{12}P_2$ is also softened when subject to e-h excitation, resulting from the bond strength reduction of the intericosahedral B-B bond and the chain P-P bond. Our calculation results indicate that excited e-h pairs significantly weaken the bond, which leads to the decrease of the strength of superhard materials.

2. COMPUTATIONAL METHODOLOGY

In this work, all the simulations were carried out using the Vienna ab initio simulation (VASP) package based on periodic and plane-wave-based codes. The pseudopotentials generated from the projector augmented wave (PAW) formalism were used to describe the interaction between ions and electrons of each atom. The electronic exchange and correlation energies were examined using generalized gradient approximation type Perdew—Burke—Ernzerhof functionals. In all DFT simulations, the cutoff value of plane waves was set

as 500 eV and the criterion of total energy error for self-consistent field iterations was 10^{-5} eV. The partial occupancy of each orbital was performed using the tetrahedron method with Blöchl correction.³⁶ The conjugate gradient method was applied to relax the ions in geometry optimization, and the force convergence for the ion relaxation was set as 10^{-3} eV/Å. To evaluate the Brillouin zone integration, the *K*-point mesh based on the Monkhorst-Pack grid approach was applied. The resolution of the *K*-point meshes in all simulations was above $2\pi \times 1/40 \text{ Å}^{-1}$.

We applied the theory of Voigt-Reuss-Hill³⁷ to explore the effects of e-h pairs on the elastic properties of B_4C and $B_{12}P_2$, through calculating the bulk modulus (K) and shear modulus (G) from the elastic constant, C_{ij} . We first performed DFT and CDFT to calculate 21 independent elastic constants C_{ij} under both ground and excited states based on the stress—strain relationship in a sufficiently small deformation range, respectively.^{37,38} Then, we used $S_{ij} = (C_{ij})^{-1}$ to calculate the stiffness constant S_{ij} .^{37,38} Finally, according to the Voigt-Reuss-Hill approximate model, the bulk modulus (K) and the shear modulus (G) could be obtained by the corresponding single-crystal C_{ij} and S_{ij} .^{37,38}

To describe the e-h excitation in superhard materials, we applied the CDFT scheme 34,35,39-43 in which the occupation of the electronic state is fixed to the particular configuration. The occupation matrix of the excited hole or electron was acquired by removing an electron from or adding an electron to the neutral system, respectively. The electron/hole occupation configuration is fixed during the structure relaxation, assuming that small structure change does not significantly influence the excited e-h configurations.

To investigate the deformation mechanism, we carried out the ideal shear deformation on B₄C along the (001)[100] slip system, which is the most plausible rhombohedral slip system. For $B_{12}P_2$, we considered three slip systems: $(011)[2\overline{11}]$, (001)[100], and (111)[1 $\overline{1}$ 0] since its plausible slip systems may differ from those of B₄C.^{30,44} In all these calculations, structure parameters are allowed to relax along all five strain components other than the imposed shear strain.⁴⁵ After relaxation, the residual stresses were less than 0.2 GPa. For the shear deformation of B_4C , we used a $2 \times 2 \times 2$ supercell with 120 atoms and employed a $(3 \times 3 \times 3)$ K-point grid mesh. For the shear deformation of B₁₂P₂, we used the supercell with 84 atoms for the $(111)[1\overline{10}]$ slip system, the supercell with 112 atoms for the $(011)[2\overline{11}]$ slip system, and the 2 × 2 × 2 supercell with 112 atoms for the (001)[100] slip system, respectively. We applied the $(4 \times 2 \times 2)$, $(3 \times 3 \times 3)$, and $(3 \times 3 \times 3)$ \times 2 \times 4) K-point grid meshes for (111)[1 $\overline{10}$], (001)[100], and $(011)[2\overline{11}]$ slip systems, respectively. The small supercell in DFT simulations leads to high carrier concentrations of ~1.15 $\times 10^{21} \text{ cm}^{-3} \text{ for B}_4\text{C and } \sim 1.02 \times 10^{21} \text{ cm}^{-3} \text{ for B}_{12}\text{P}_{2}$, which corresponds to the highly doped semiconductors. 46-4

All crystal orbital Hamilton population (COHP)⁴⁹ analyses in this work were executed in the LOBSTER package. ^{49,50} The COHP can be used to investigate the chemical bonding information, which is based on PAW output from the VASP code. The COHP refers to partitioning the band structure energy in terms of the contributions of orbital pairs. The bonding (i.e., negative value), antibonding (i.e., positive value), and nonbonding (i.e., zero values) regions in the range of a specific energy can be obtained through COHP analysis. Projected COHP (pCOHP) allows the chemical bond to be projected from plane waves. In addition, the integrated

Table 1. Elastic Moduli (K and G) of B_4C and $B_{12}P_2$ under the 0h0e and 1/4 e-h Pair Excited States, Respectively^a

	$K_{ m V}$	$G_{ m V}$	$K_{ m R}$	$G_{ m R}$	K	G
B_4C	238.61	202.96	236.98	194.87	237.79	198.92
$B_4C + 1/4e-h$ pairs	233.01	201.50	230.29	189.88	231.65	195.69
$B_{12}P_{2}$	199.89	191.27	198.50	190.60	199.19	190.64
$B_{12}P_2 + 1/4e-h$ pairs	196.34	180.25	192.66	179.30	194.50	179.78

"The K_V and G_V represent the bulk modulus and shear modulus for the Voigt average, respectively. The K_R and G_R represent the bulk modulus and shear modulus for the Reuss average, respectively (unit: GPa).

pCOHP (IpCOHP) can be applied to determine the bond strength by calculating the integral from the initial band energy to the Fermi energy. A higher value of IpCOHP suggests a higher bond strength. To evaluate the electron and hole distribution under e-h excitation, the charge density difference between the e-h excited states and the ground state was calculated. We carried out the electron localization function (ELF) to probe the bonding breaking and rearrangement during the shear deformation. The value of the ELF isosurface is 0.85. The visualization software VESTA⁵² was used to display the crystal structure, ELF analysis, and charge density difference.

3. RESULTS AND DISCUSSION

3.1. Crystal Structure under e-h Excited States. B₄C and $B_{\underline{12}}P_2$ have a similar crystal structure, both belonging to the $R\overline{3}m$ space group 23,44 Previous studies revealed that B_4C consists of a B₁₁C icosahedron cluster and C-B-C chain connected to the icosahedron along the [111] direction.²³ The extra polyhedral bonds of B₁₁C can be regarded as two-centertwo-electron (2c-2e) bonds, and the middle B atom in the C-B-C chain would provide one electron to participate in the internal bonding of B₁₁C, making 26 electrons delocalized in the B₁₁C icosahedron and leading to the formula of $(B_{11}C)^{1-}[C-B^+-C]$ for B_4C . The equilibrium lattice parameters given by DFT simulations are a = b = 5.207 Å, c = 5.057Å, $\alpha = \beta = 113.98^{\circ}$, and $\gamma = 65.14^{\circ}$. The lattice parameters are changed to $a = b = 5.206 \text{ Å}, c = 5.061 \text{ Å}, \alpha = \beta = 113.96^{\circ}, \text{ and}$ $\gamma = 65.19^{\circ}$ under e-h pair excitation with an e-h concentration of 1.15×10^{21} cm⁻³, suggesting that the lattice constants are barely changed.

The B₁₂P₂ single crystal has a rhombohedral unit cell similar to that of B₄C but with the B₁₂ icosahedron and the P–P chain along the [111] direction. The P atom in the P–P chain provides one electron to involve in the internal bonding of B₁₂ icosahedra, becoming P⁺, resulting in a formula of (B₁₂)^{2–}[P⁺– P⁺], satisfying Wade's rule.⁵³ Our DFT simulations give the equilibrium lattice parameters a = b = c = 5.252 Å and $\alpha = \beta = \gamma = 69.58^{\circ}$. The lattice constants are changed to a = b = c = 5.251 Å and $\alpha = \beta = \gamma = 69.64^{\circ}$ under e-h excited states with a concentration of ~1.02 × 10²¹ cm⁻³, suggesting that the e-h excitation does not have a significant influence on the lattice constants of B₁₂P₂.

It is expected that the e-h excitations will have an impact on the elastic properties of B_4C and $B_{12}P_2$. Therefore, we used the theory of Voigt-Reuss-Hill to investigate this effect. Table 1 lists the computed results of the bulk modulus (K) and the shear modulus (G) of the ground state and excited state with 1/4 e-h pairs. For B_4C , the K and G of the excited state with 1/4 e-h pairs decrease by 2.65 and 1.62% compared to the ground state, respectively, indicating that e-h pairs weaken B_4C . The same trend also appears in $B_{12}P_2$. 1/4 e-h pair

excitation leads to a decrease of K and G by 2.41 and 5.70%, respectively, suggesting that e-h pairs also weaken $B_{12}P_2$.

3.2. Amorphization of B_4C under e-h Excitation. To illustrate the deformation mechanism of B_4C under e-h excitation, we applied the ideal shear deformation along the (001)[100] slip system since it is the most plausible slip system. Previous TEM experiments have established the formation of the amorphization along this (001)[100] slip system. Recent DFT simulations confirmed that the ideal shear strength for this slip system is the lowest among all 11 plausible slip systems. To illustrate the effects of carrier concentration (n_i) , we consider two e-h concentrations: 1h-1e per supercell $(1.15 \times 10^{21} \text{ cm}^{-3})$ and 2h-2e per supercell $(2.29 \times 10^{21} \text{ cm}^{-3})$.

The stress-strain curves of B₄C for the slip system (001) [100] under the ground state and e-h excited states are shown in Figure 1. The 0h0e, 1h1e, and 2h2e denote the ground state,

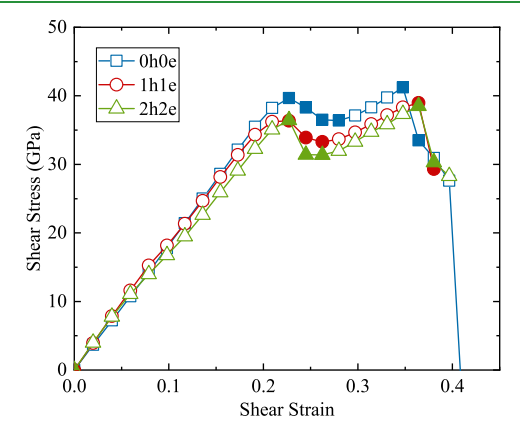


Figure 1. Stress—strain curves of B₄C for the (001)[100] slip system under the two e-h pair excited state (2h2e), the one e-h pair excited state (1h1e), and the ground state (0h0e), respectively. The key failure steps displayed by the filled symbols are shown in Figures 2, S1, and S2.

one e-h pair excited in the supercell ($n_i \sim 1.15 \times 10^{21}$ cm⁻³), and two e-h pairs excited in the supercell ($n_i \sim 2.29 \times 10^{21}$ cm⁻³), respectively. With 1h–1e, the ideal shear strength of B₄C drops to 38.98 GPa compared to 41.22 GPa at 0h0e, decreasing by 5.43%. Meanwhile, the critical failure strain increases from 0.348 to 0.364. Therefore, excited e-h pairs reduce the strength but enhance the ductility of B₄C. The carrier concentration also influences the strength of B₄C. As the n_i increases to 2.29×10^{21} , the ideal shear strength further decreases to 38.51 GPa, while the critical shear stress remains 0.364, indicating that a higher e-h concentration decreases the ideal shear stress. Notably, the slope of the stress—strain relations of excited states decreases in the elastic deformation region (shear strain <0.1), indicating that the shear modulus also decreases under e-h excitation. This is consistent with the

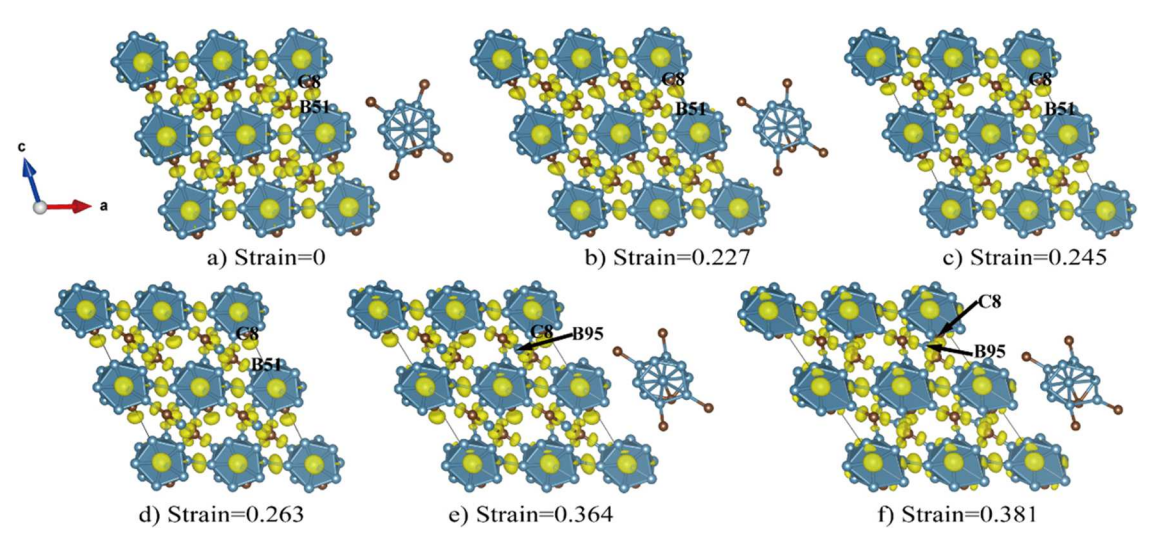


Figure 2. Structural evolution of the B_4C system along (001)[100] shear under the 1h1e excited state: (a) intact structure; (b) structure deforms elastically at a shear strain of 0.227; (c) at a shear strain of 0.245, the C8-B51 bond breaks; (d) no icosahedra are destroyed at a shear strain of 0.263; (e) at 0.381 shear strain, the stress reaches the maximum value; (f) failure starts by the cage C8 reacting with the chain B95 at a shear strain of 0.397. Indigo and sienna balls, respectively, represent the B and C atoms. A yellow isosurface represents the ELF with a value of 0.85.

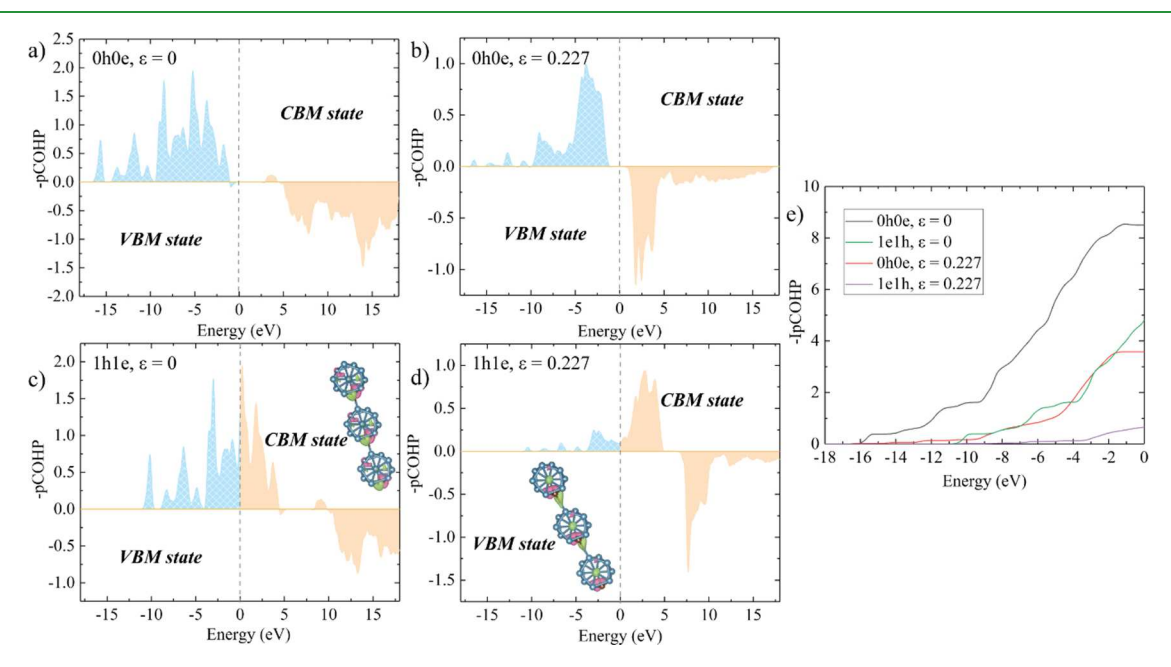


Figure 3. pCOHP analysis for the C8–B51 bond between icosahedra under the 1h1e state and 0h0e state: (a) at a strain of 0.0, the intact structure under the 0h0e state; (b) at a strain of 0.227, the deformed structure under the 0h0e state; (c) at a strain of 0.0, the intact structure under the 1h1e state; (d) at a strain of 0.227, the deformed structure under the 1h1e state; (e) IpCOHP for C8–B51 bonds between icosahedra under the 1e1h state and 0h0e state. The charge density difference for the perfect structure and deformed structure between the 1h1e state and 0h0e state is inserted in (c) and (d), respectively. The electronic orbitals of the conduction band minimum (CBM) are marked by light orange, and those of valence band maximum (VBM) are marked by blue; and the hole and electronic densities caused by e-h excitation are marked by light green and lavender, respectively.

elastic modulus prediction in which the elastic modulus of e-h excited B_4C is lower than that under the ground state. This suggests that the e-h pairs affect the speed of sound in semiconductors and may influence the thermal transport properties. ⁵⁴

The shear-induced failure mechanism of B_4C along the (001)[100] slip system under the 0h0e state is shown in Figure S1 and has been discussed in previous studies. First, the B-C bond between icosahedra is broken under shear, resulting in the carbene forming a lone pair. With the increase of the shear strain, the B atom in the C-B-C chain interacts with the

carbene, leading to the deconstruction of icosahedra, which accounts for the brittle failure.

Figure 2 displays the crucial structural evolution for the shear-induced failure mechanism of B_4C along the (001)[100] slip system under the 1h1e state. The isosurface of ELF [49, 50] is plotted to assess the bonding breaking or rearrangements under shear deformation. The intact structure, displayed in Figure 2a, is subject to elastic deformation until reaching the 0.227 shear strain (Figure 2b). The C8–B51 bond between neighboring icosahedra is stretched during the elastic deformation, but the ELF suggests that it is not broken. The

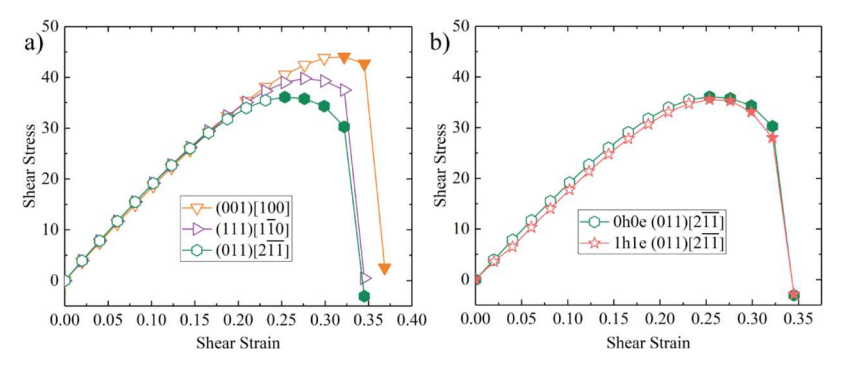


Figure 4. (a) Stress—strain curves of $B_{12}P_2$ for $(011)[2\overline{11}]$, (001)[100], and $(111)[1\overline{10}]$ slip systems under shear deformation; (b) stress—strain curves for the $(011)[2\overline{11}]$ slip system under 0h0e and 1h1e states, respectively. The key failure steps displayed by the filled symbols are shown in Figures 5 and 8.

bond distance of C8-B51 increases to 2.574 Å as the shear strain increases to 0.245 (Figure 2c), breaking the bonds and forming a lone pair on cage C. The pair electron is located at the C8 atom, indicating a lone pair electron. No icosahedra are deconstructed at 0.263 shear strain, as plotted in Figure 2d. At 0.364 shear strain (Figure 2e), corresponding to the maximum shear stress of 38.98 GPa, the C-B-C chain moves closer to the carbene formed at a shear strain of 0.245 due to the intericosahedral bond breaks. With the shear strain further increasing to 0.381 (Figure 2f), the icosahedra are deconstructed by forming a new bond between the carbene (C8) and the middle chain B (B95). This failure mechanism is the same as the ground state, indicating that the failure mechanism is unaffected by e-h pairs along this slip system. However, the lower ideal shear strength and higher failure strain suggested the relatively low material strength and higher deformation capability of B₄C under e-h excitation. Under the 2h2e state, the deformation process for the (001)[100] slip system remains the same with the 1h1e state and 0h0e state, as illustrated in Figure S2.

The e-h excitation has a noticeable effect on the failure strain and ideal strength of B₄C. To understand this phenomenon, we performed pCOHP analysis to investigate the bonding information and bond strength. A positive crystal orbital overlap population (COOP) denotes a bonding state, while a negative COOP denotes an antibonding state.⁵¹ Here, we take -pCOHP to be consistent with the COOP method. Figure 3a,b shows the -pCOHP of the intact (0.0 shear strain) and the deformed (0.227 shear strain) structures under the 0h0e state and 1h1e state, respectively. The charge density difference between the 1h1e and 0h0e states is also displayed to illustrate the modified electron (hole) distribution under e-h excitation. The -pCOHP of the C8-B51 bond between neighboring icosahedra was calculated because it breaks first under shear deformation and causes structural destruction. For both intact and deformed structures, we also integrated the -pCOHP of the C8-B51 bond to determine the change of bond strength with e-h excitation. Figure 3a,b shows the bonding and antibonding characters for the intact and deformed structures under the 0h0e state, respectively. Moreover, there is a bandgap between the valence and conduction bands. Figure 3c,d displays the bonding and antibonding characters of the initial and deformed structures at the 1h1e state, respectively. With the excited e-h pairs, the electrons near VBM will transfer from the bonding states to the antibonding states and create the excess electron and hole states, which are represented by lavender and light green isosurfaces, respectively. This results

in that the Fermi level touches the bonding state for both intact and deformed structures. In addition to *p*COHP analysis, we also calculated the charge density difference between 1h1e and 0h0e states for both intact and deformed structures, respectively, as shown in Figure 3c,d. The hole state is distributed among the B–C bonds between icosahedra. On the contrary, the excess electron state is distributed within the cage, indicating that electron transfers from the intericosahedral bond to the cage, weakening the intericosahedral bonding and lowering the shear strength for the initial bond breaking between icosahedral—icosahedral B–C bonds. To confirm this, Figure 3e shows that the value of -IpCOHP is lower under the 1h1e state, suggesting that the e-h excitation decreases the bond strength.

3.3. The Effect of Electronic Excitation on $B_{12}P_2$. Previous theoretical studies suggested that $B_{12}P_2$ can suppress the deconstruction of icosahedral clusters because the P-P chain facilitates the icosahedral slip under shear deformation, releasing the accumulated shear stress. Therefore, the perfect crystalline $B_{12}P_2$ may be a ductile and hard material. It will be interesting to examine the e-h excitation on this system with a different deformation mechanism but a similar crystal structure to B_4C . To elucidate how e-h excitation affects the intrinsic failure mechanism of $B_{12}P_2$, we carried out the ideal shear deformation on $B_{12}P_2$ under the ground state (0h0e) and excited states (1h1e and 2h2e).

To determine the most plausible slip system, we first examined the shear deformation along three possible slip systems of (011)[211], (001)[100], and (111)[110]. Figure 4a displays the stress-strain curves of these three slip systems under ideal shear deformation. The ideal shear strength is 44.02, 39.77, and 36.09 GPa for (001)[100], $(111)[1\overline{1}0]$, and $(011)[2\overline{11}]$, respectively. Our results show that the ideal shear strength for the slip system $(011)[2\overline{11}]$ is the lowest among other slip systems. This implies that the slip system (011) [211] is the most plausible slip system for $B_{12}P_2$, which is different from B_4C with the most plausible slip of (001)[100]. Hence, we focused on the deformation mechanism of B₁₂P₂ along $(011)[2\overline{11}]$ to understand the effect of e-h excitation on the failure mechanism. Figure 4b plots the stress-strain curves of $B_{12}P_2$ along the $(011)[2\overline{11}]$ slip system under the ground state (0h0e state) and 1h-1e excited state. $B_{12}P_2$ deforms elastically under both 0h0e and 1h1e states as the shear strain is less than 0.1. The slope of the stress-strain curve is lower for the 1h1e state than for the 0h0e state, indicating that the e-h excitation slightly lowers the shear modulus of B₁₂P₂. This agrees with the elastic modulus prediction in which the e-h

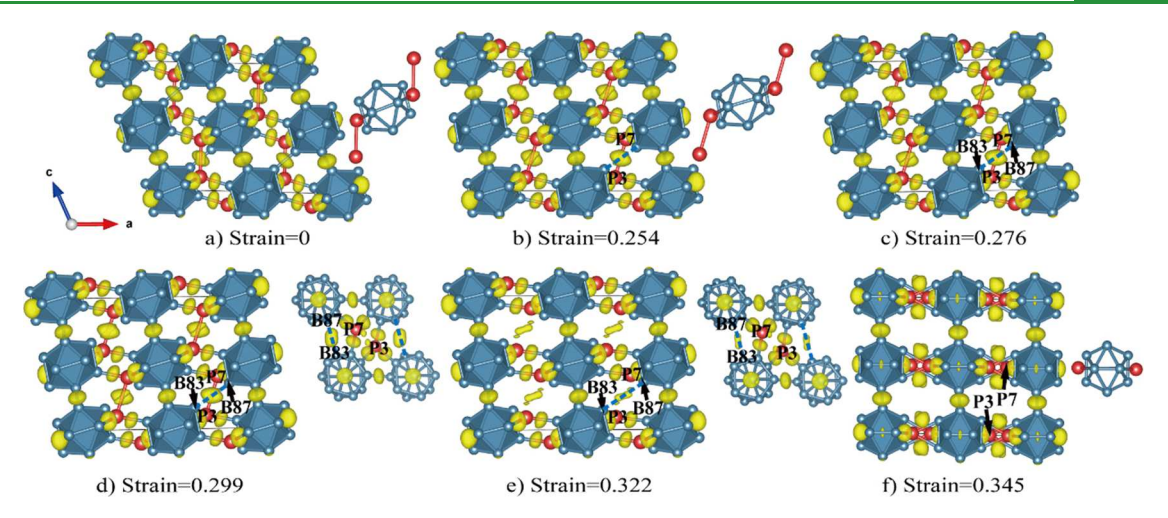


Figure 5. Structural evolution of $B_{12}P_2$ along the $(011)[2\overline{11}]$ slip system at the excited state with 1h1e: (a) intact structure; (b) shear stress reaches the maximum value at a shear strain of 0.254; (c) at 0.276 shear strain, no bonds break in the structure; (d) at a shear strain of 0.299, the chain P3–P7 bond and the B83–B87 bond between icosahedra are stretched but not broken; (e) at a shear strain of 0.322, the chain P3–P7 bond is broken and the B83–B87 bond starts to break; (f) no icosahedron fractured at a shear strain of 0.345. The blue and red balls in the figure, respectively, denote the B and P atoms. A yellow isosurface represents the ELF with a value of 0.85.

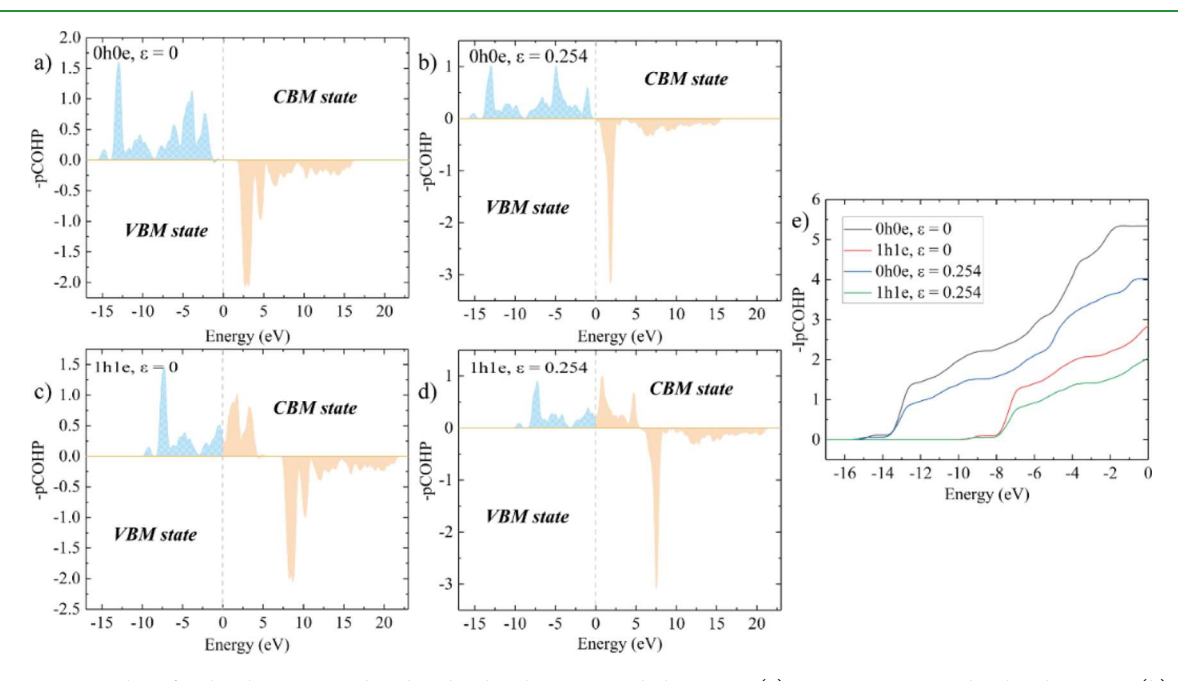


Figure 6. pCOHP analysis for the chain P3-P7 bond under the 1h1e state and 0h0e state: (a) intact structure under the 0h0e state; (b) deformed structure (0.254 shear strain) under the 0h0e state; (c) intact structure under the 1h1e state; (d) deformed structure (0.254 shear strain) under the 1h1e state; (e) IpCOHP for the intericosahedral P3-P7 bond under the 1e1h state and 0h0e state. The electronic orbitals of the conduction band minimum (CBM) are marked by light orange, and those of the valence band maximum (VBM) are marked by blue.

pairs weaken $B_{12}P_2$. Additionally, the ideal shear strength for the 1h1e state is 35.53 GPa at 0.254 critical strain, which is 1.55% lower than the critical shear stress (36.09 GPa) for the 0h0e state. This indicates that e-h excitation weakens the strength of $B_{12}P_2$, which is similar to B_4C .

We examined the detailed failure mechanism of $B_{12}P_2$ along $(011)[2\overline{11}]$ under both the 0h0e state and 1h1e state. Figure 5 shows the structural changes and the ELF analysis at various important strains of $B_{12}P_2$ under the 1h1e state $(n_i \sim 1.02 \times 10^{21} \text{ cm}^{-3})$. Figure 5a shows the intact structure with the P-P bond in the chain. The isosurface of ELF analysis confirms this P-P bond. The structure deforms elastically with continued shear strain. Particularly, at a strain of 0.254 (Figure 5b), the ideal shear stress reaches the maximum value. Figure 5c

corresponding to the structure at 0.276 shear strain shows that the P3–P7 chain bond is stretched from 2.390 to 2.436 Å, while the B83–B87 intericosahedral bond is also stretched from 2.370 to 2.526 Å. However, the ELF shows that both of them are not broken. Then, at a shear strain of 0.299 (Figure 5d), the distances of P3–P7 and B83–B87 bonds are further increased to 2.519 and 2.758 Å without breaking, respectively. No isosurface exists between P3 and P7 atoms as the shear strain further increases to 0.322 (Figure 5e), suggesting that the P3–P7 bond is broken. Meanwhile, the distance of the B83–B87 bond is drastically increased to 3.041 Å, indicating this bond starts to break. After this, at 0.345 shear strain, each P atom in the P–P chain interacts with one B atom in the B₁₂ icosahedron without fracturing the icosahedra, as displayed in

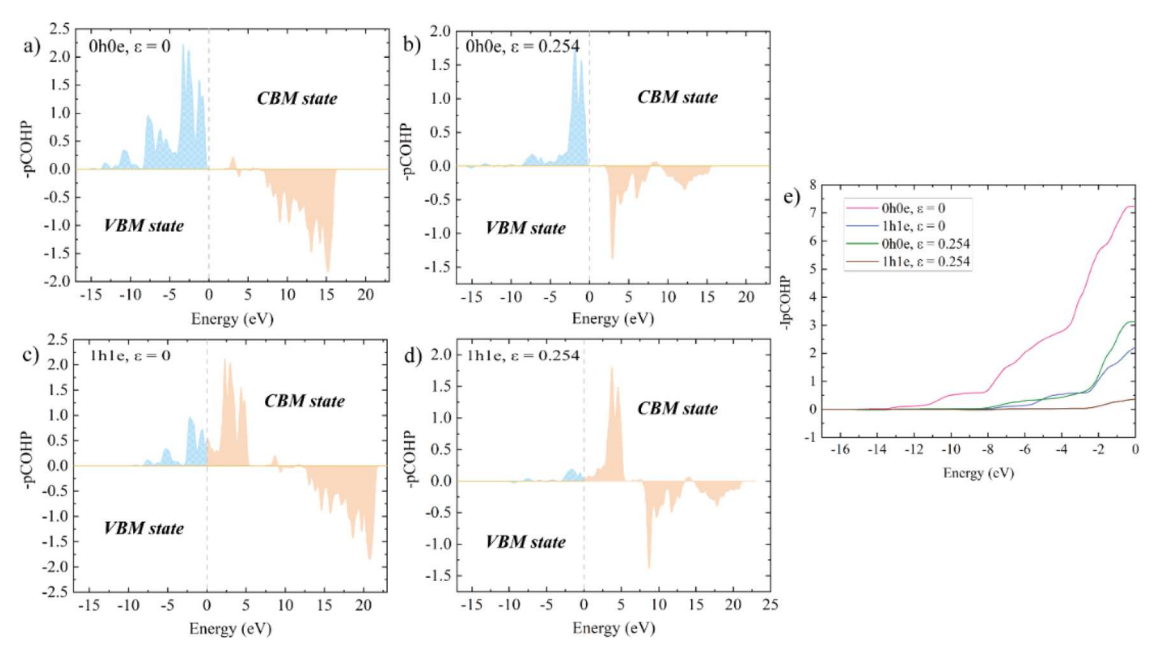


Figure 7. pCOHP analysis for the chain B83–B87 bond under the 1h1e state and 0h0e state: (a) intact structure under the 0h0e state; (b) deformed structure (0.254 shear strain) under the 0h0e state; (c) intact structure under the 1h1e state; (d) deformed structure (0.254 shear strain) under the 1h1e state; (e) IpCOHP for the intericosahedral P3–P7 bond under the 1e1h state and 0h0e state. The electronic orbitals of the conduction band minimum (CBM) are marked by light orange, and those of the valence band maximum (VBM) are marked by blue.

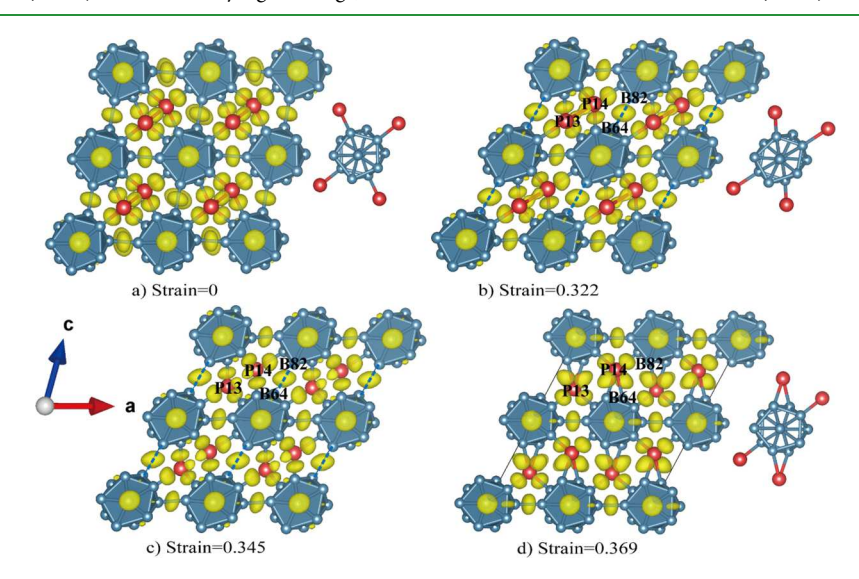


Figure 8. Structural changes of $B_{12}P_2$ for the slip system (001)[100] under the 1h1e excited state: (a) intact structure; (b) at 0.322 shear strain, the shear stress achieved the maximum value; (c) at a shear strain of 0.345, the chain P13–P14 bond is broken; (d) B64–B82 bond between neighboring icosahedra is broken at 0.369 shear strain. Blue and red balls in the figures, respectively, represent the B and P atoms. A yellow isosurface represents the ELF with a value of 0.85.

Figure 5f. Notably, under the 0h0e state, $B_{12}P_2$ exhibits the same failure process as the 1h1e state, as shown Figure S3. These results suggest that the breaking of both P–P chains and intericosahedral B–B bonds initiates the structural failure of $B_{12}P_2$ under both the ground state and excited states.

Next, we performed pCOHP analysis to analyze the origin of the effects of e-h excitation on the mechanical behavior of $B_{12}P_2$. Here, we focused on the P3-P7 chain and intericosahedral B83-B87 bonds since they break first under shear deformation and initiate structural failure. In particular, the obtained -pCOHP curves of these two bonds in both intact (0.0 strain) and deformed (0.254 strain) structures under the 0h0e state and 1h1e state are shown in Figures 6 and 7,

respectively. Under the 0h0e state, the valence and conduction bands of P3–P7 and B83–B87 bonds are composed of bonding and antibonding states in both intact and deformed structures, as displayed in Figure 6a,b and Figure 7a,b, respectively. When the e-h excitation happens, the electrons near VBM will transfer from the bonding states to the antibonding states and create e-h pairs. Thus, the Fermi level touches their bonding states of both intact and deformed structures under the 1h1e state, as shown in Figure 6c,d and Figure 7c,d, respectively. More importantly, for both intact and deformed structures, the -IpCOHPs of P3–P7 and B83–B87 bonds under the 1h1e state are lower than those under the 0h0e state, as shown in Figure 6e and Figure 7e, respectively.

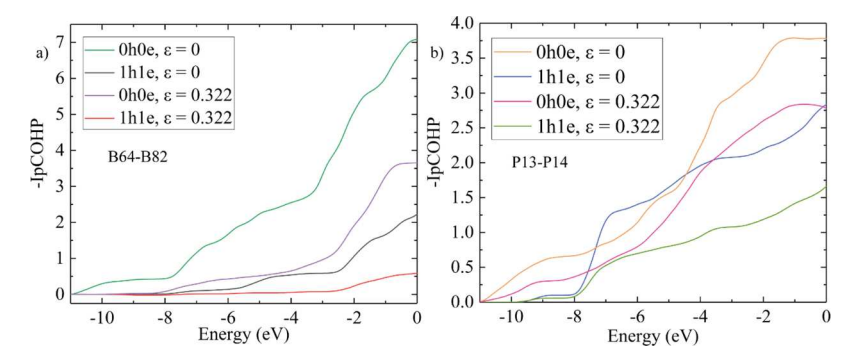


Figure 9. IpCOHP for (a) intericosahedral B64-B82 bond under 1h1e and 0h0e states and (b) chain P13-P14 bond under 1h1e and 0h0e states.

This suggests that excited e-h pairs weaken these two bonds, decreasing ideal shear strength under the 1h1e state.

To further illustrate that the excited e-h pairs have an effect on the mechanical properties of B₁₂P₂, we examined the shear deformation along (001)[100] under 0h0e, 1h1e, and 2h2e states. Two e-h concentrations including 1h-1e ($n_i \sim 1.02 \times$ 10^{21} cm^{-3}) and $2\text{h}-2\text{e} (n_i \sim 2.03 \times 10^{21} \text{ cm}^{-3})$ are considered to investigate the effect of carrier concentrations. The stressstrain curves of the slip system (001)[100] under the ground state and excited states (1h-1e and 2h-2e) are plotted in Figure S4. Under the 1h1e state $(n_i \sim 1.02 \times 10^{21} \text{ cm}^{-3})$, the ideal shear stress of B₁₂P₂ is 43.00 GPa at 0.322 strain, which is 2.32% lower than 44.02 GPa under the 0h0e state at the same strain, suggesting that the e-h excitation weakens its strength. However, under the 2h2e state $(n_i \sim 2.03 \times 10^{21} \text{ cm}^{-3})$, the ideal shear strength (43.12 GPa) is slightly higher than that under the 1h1e state, suggesting that a higher carrier concentration might lead to the increase of ideal shear strength. The critical strain under the 2h2e state (0.345) is also larger than that of 1h1e and ground states (0.322). This indicates that higher carrier concentrations can slightly improve the ductility of $B_{12}P_2$. In addition, in the elastic range (<0.1), the slopes of stress-strain curves for both excited states (1h-1e and 2h-2e) are lower compared to the ground state, suggesting that the shear modulus decreases under e-h excitation, which is the same with B₄C. This result is in accordance with elastic modulus prediction.

In order to illustrate the effect of e-h pairs on the failure mechanism, the ELF analysis results of structures at various critical strains of $B_{12}P_2$ under 1h1e states ($n_i \sim 1.02 \times 10^{21}$ cm⁻³) are shown in Figure 8. The intact structure is shown in Figure 8a, and the ELF indicates that the P-P bond forms the chain. The chain P13-P14 bond is stretched from 2.268 to 2.468 Å as the shear strain increases to 0.322. Meanwhile, the distance of the intericosahedral B64-B82 bond is increased from 1.747 to 2.222 Å, as shown in Figure 8b. However, the ELF shows that both of them are not broken. In Figure 8c, the chain P13-P14 bond stretches to 2.529 Å and breaks at 0.345 shear strain. In addition, the B64-B82 bond between icosahedra is also stretched to 2.351 Å. However, the isosurface between B64 and B82 atoms still exists at this strain, suggesting that it is not broken. Then, the B64-B82 bond breaks as the shear strain increases to 0.369 (Figure 8d), decreasing the shear stress from 41.61 to 1.97 GPa. Meanwhile, each P atom interacts with three icosahedra, forming four bonds, and no bond within icosahedra breaks. Similar to the 1h1e state, the failure mechanism of B₁₂P₂ under 0h0e and 2h2e states also arises from the breaking of the P-P chain and the B-B bond between icosahedra, as plotted in Figures S5 and S6, respectively. Thus, it is vital to understand how e-h pairs affect the P-P chain bond and intericosahedral B-B bond in the process of the shear deformation along (001)[100].

The pCOHP technique was performed to manifest the changes of strengths for P13–P14 and intericosahedral B64– B82 bonds under the e-h excitation, as plotted in Figures S7 and S8. Under the 0h0e state, the valence and conduction bands of B64-B82 and P13-P14 bonds are composed of bonding and antibonding states in both intact and deformed structures, as plotted in Figures S7a,b and S8a,b, respectively. Under the 1h1e state, their Fermi level touches the bonding states of intact and deformed structures, as is shown in Figures S7c,d and S8c,d, respectively. To better illustrate the effects of e-h pairs on bond strengths, the -IpCOHPs of B82-B64 and P13-P14 bonds under the 1h1e state were also investigated and compared with -IpCOHPs under the 0h0e state, as plotted in Figure 9. For both intact and deformed structures, the bond strengths of these two bonds under the 1h1e state are lower than those under the 0h0e state, indicating that e-h pairs weaken both intericosahedral B-B and P-P bonds, which accounts for the reduction of ideal shear strength under excited states.

Our results show that the softening from e-h pair excitation in B₁₂P₂ is less than that in B₄C. The ideal shear strength of B₄C is reduced by 5.43% under the 1h1e state compared to the ground state, which is higher than the reductions of ideal shear strength of $B_{12}P_2$ under the 1h1e state (2.32% for (001)[100] and 1.55% for $(011)[2\overline{11}]$). The mechanism beyond that can be explained by our IpCOHP analyses on bonds that break first and initiate the structural failure. At critical strain before structural failure, the bond strength of the C8-B51 bond in B_4C decreases by 81.63% under the 1h1e state. For $B_{12}P_{2}$, when shear is along (011)[211], the bond strength of the P3-P7 bond only decreases by 49.58% under the 1h1e state. Besides, when shear is along (001)[100], the bond strength of the P13-P14 bond decreases by 40.17% under the 1h1e state. These two values are much smaller than those of B₄C. These results suggest that the excited e-h pairs transfer more electrons in B₄C than in B₁₂P₂, causing more apparent softening effects in B_4C .

4. CONCLUSIONS

The present work was undertaken to evaluate the effects of e-h excitations on superhard materials of B_4C and $B_{12}P_2$ by using constrained DFT simulations. Our results indicate that e-h excitations lower both the shear modulus and the ideal shear strength of B_4C and $B_{12}P_2$. These results are consistent with the elastic modulus prediction, e-h pairs leading to a decrease of both K and G. The microscopic origin for this effect is that

the excited e-h pairs reduce the strengths of bonds during the shear deformation and initiate structural failure. For B₄C, the structural failure starts from breaking the B-C bond between icosahedra. Under excited states, the excited electrons transfer from intericosahedral B-C bonds to B₁₁C icosahedra, weakening the intericosahedral B-C bonds and thus lowering the ideal strength of B_4C . For $B_{12}P_2$, the failure mechanism shearing along $(011)[2\overline{11}]$ and (001)[100] is due to the breaking of both P-P chains and intericosahedral B-B bonds. Under excited states, these two bonds are weakened. Therefore, the ideal strengths of B₁₂P₂ under excited states are lower compared to the ground state. Overall, our study offers an atomistic understanding of the mechanical properties of superhard B₄C and B₁₂P₂ under e-h excitations. This study also provides the basis for tuning the mechanical properties of superhard materials through external fields.

ASSOCIATED CONTENT

Supporting Information

The Supporting Information is available free of charge at https://pubs.acs.org/doi/10.1021/acsami.2c05528.

Failure mechanism of B₄C along the slip system (001) [100] under the 0h0e state (Figure S1); failure mechanism of B₄C along the slip system (001)[100] under the 2h2e state (Figure S2); failure mechanism of $B_{12}P_2$ along the slip system $(011)[2\overline{11}]$ under the 0h0e state (Figure S3); the stress-strain curves for the slip system (001)[100] under 0h0e, 1h1e, and 2h2e states (Figure S4); failure mechanism of B₁₂P₂ along the slip system (001)[100] under the 0h0e state (Figure S5); failure mechanism of B₁₂P₂ along the slip system (001) [100] under the 2h2e state (Figure S6); Figure S7 showing the pCOHP analysis for the B64-B82 bond under 0h0e and 1h1e states; and Figure S8 showing the pCOHP analysis for the chain P13-P14 bond under 0h0e and 1h1e states (PDF)

AUTHOR INFORMATION

Corresponding Authors

Bin Tang - State Key Laboratory of Electronic Thin Films and Integrated Devices, University of Electronic Science and Technology of China, Chengdu 610054, China;

orcid.org/0000-0002-3851-2330; Email: tangbin@ uestc.edu.cn

Qi An - Department of Chemical and Materials Engineering, University of Nevada-Reno, Reno, Nevada 89557, United States; o orcid.org/0000-0003-4838-6232; Email: qia@ unr.edu

Authors

Yi He - State Key Laboratory of Electronic Thin Films and Integrated Devices, University of Electronic Science and Technology of China, Chengdu 610054, China

Yidi Shen – Department of Chemical and Materials Engineering, University of Nevada-Reno, Reno, Nevada 89557, United States

Complete contact information is available at: https://pubs.acs.org/10.1021/acsami.2c05528

Notes

The authors declare no competing financial interest.

ACKNOWLEDGMENTS

Y.S. and Q.A. were supported by the National Science Foundation (CMMI-1727428).

REFERENCES

- (1) Lambrecht, W. Dopants and Defects in Semiconductors. *Mater.* Today 2012, 15, 349.
- (2) Osip'yan, Y.; Savchenko, I. Experimental Observation of The Influence of Light on Plastic Deformation of Cadmium Sulfide. JETP Lett. 1968, 7, 100.
- (3) Maeda, K.; Takeuchi, S. Chapter 54 Enhancement of Dislocation Mobility in Semiconducting Crystals by Electronic Excitation. In Dislocations in Solids, Nabarro, F. R. N., Duesbery, M. S. Eds.; Elsevier, 1996; 10; 443-504.
- (4) Carlsson, L.; Svensson, C. Photoplastic Effect in ZnO. J. Appl. Phys. 1970, 41, 1652-1656.
- (5) Carlsson, L.; Ahlquist, C. N. Photoplastic Behavior of CdTe. J. Appl. Phys. 1972, 43, 2529-2536.
- (6) Choi, S. K.; Mihara, M.; Ninomiya, T. Dislocation Velocities in GaAs. Jpn. J. Appl. Phys. 1977, 16, 737-745.
- (7) Levade, C.; Couderc, J. J.; Vanderschaeve, G.; Caillard, D.; Couret, A. TEM Insitu Observation of Recombination-Enhanced Mobility of Dislocations in II-VI Compounds. Appl. Surf. Sci. 1991, 50, 119-124.
- (8) Levade, C.; Vanderschaeve, G. Electron-Irradiation Enhanced Dislocation Glide in II-VI Semiconductors. J. Cryst. Growth 1999, 197, 565-570.
- (9) Werner, M.; Bartsch, M.; Messerschmidt, U.; Baither, D. TEM Observations of Dislocation Motion in Polycrystalline Silicon During in Situ Straining in the High Voltage Electron Microscope. phys. stat. sol. (a) 1994, 146, 133-143.
- (10) Oshima, Y.; Nakamura, A.; Matsunaga, K. Extraordinary Plasticity of an Inorganic Semiconductor in Darkness. Science 2018, 360, 772-774.
- (11) Wang, H.; Morozov, S. I.; Goddard, W. A.; An, Q. Light Irradiation Induced Brittle-to-Ductile and Ductile-to-Brittle Transition in Inorganic Semiconductors. Phys. Rev. B 2019, 99, No. 161202.
- (12) Maeda, K.; Suzuki, K.; Ichihara, M.; Takeuchi, S. Electron-Beam Irradiation Enhanced Dislocation Glide in GaAs Observed by Transmission Electron Microscopy. J. Appl. Phys. 1984, 56, 554-556.
- (13) Callahan, P. G.; Haidet, B. B.; Jung, D.; Seward, G. G. E.; Mukherjee, K. Direct Observation of Recombination-Enhanced Dislocation Glide in Heteroepitaxial GaAs on Silicon. Phys. Rev. Mater. 2018, 2, No. 081601.
- (14) Maeda, K.; Takeuchi, S. Enhanced Glide of Dislocations in GaAs Single Crystals by Electron Beam Irradiation. Jpn. J. Appl. Phys. 1981, 20, L165-L168.
- (15) Maeda, K.; Takeuchi, S. Recombination Enhanced Dislocation Glide in InP Single Crystals. Appl. Phys. Lett. 1983, 42, 664-666.
- (16) Wang, H.; Song, S.; Zou, X.; Wang, F.; Zhang, Z.; Morozov, S. I.; Wang, X.; Reddy, K. M.; An, Q. Photomechanical Effect Leading to Extraordinary Ductility in Covalent Semiconductors. Phys. Rev. B 2019, 100, No. 094110.
- (17) Lagrenaudie, J. A Study of the Properties of Boron. J. Phys. Radium 1953, 14, 14-18.
- (18) Wang, H.; An, Q. Band-Gap Engineering in High-Temperature Boron-Rich Icosahedral Compounds. J. Phys. Chem. C 2019, 123, 12505-12513.
- (19) Peret, J. L. Preparation and Properties of the Boron Phosphides. J. Am. Ceram. Soc. 1964, 47, 44-46.
- (20) Takigawa, M.; Hirayama, M.; Shohno, K. Hetero-Epitaxial Growth of Boron Monophosphide on Silicon Substrate Using B2H6-PH₃-H₂ System. Jpn. J. Appl. Phys. 1974, 13, 411-416.
- (21) Varley, J. B.; Lordi, V.; Miglio, A.; Hautier, G. Electronic Structure and Defect Properties of B₆O from Hybrid Functional and Many-Body Perturbation Theory Calculations: A Possible Ambipolar Transparent Conductor. Phys. Rev. B 2014, 90, No. 045205.

- (22) Reddy, K. M.; Guo, D.; Song, S.; Cheng, C.; Han, J.; Wang, X.; An, Q.; Chen, M. Dislocation-Mediated Shear Amorphization in Boron Carbide. Sci. Adv. 2021, 7, No. eabc6714.
- (23) Domnich, V.; Reynaud, S.; Haber, R. A.; Chhowalla, M. Boron Carbide: Structure, Properties, and Stability Under Stress. J. Am. Ceram. Soc. 2011, 94, 3605-3628.
- (24) Kaner, R. B.; Gilman, J. J.; Tolbert, S. H. Designing Superhard Materials. Science 2005, 308, 1268-1269.
- (25) Chen, M.; McCauley, J. W.; Hemker, K. J. Shock-Induced Localized Amorphization in Boron Carbide. Science 2003, 299, 1563-
- (26) Reddy, K. M.; Liu, P.; Hirata, A.; Fujita, T.; Chen, M. W. Atomic Structure of Amorphous Shear Bands in Boron Carbide. Nat. Commun. 2013, 4, 2483.
- (27) Chen, M.; McCauley, J. W. Mechanical Scratching Induced Phase Transitions and Reactions of Boron Carbide. J. Appl. Phys. 2006, 100, 123517.
- (28) Domnich, V.; Gogotsi, Y.; Trenary, M.; Tanaka, T. Nanoindentation and Raman Spectroscopy Studies of Boron Carbide Single Crystals. Appl. Phys. Lett. 2002, 81, 3783-3785.
- (29) Yan, X. Q.; Li, W. J.; Goto, T.; Chen, M. W. Raman Spectroscopy of Pressure-Induced Amorphous Boron Carbide. Appl. Phys. Lett. 2006, 88, 131905.
- (30) An, Q.; Goddard, W. A.; Cheng, T. Atomistic Explanation of Shear-Induced Amorphous Band Formation in Boron Carbide. Phys. Rev. Lett. 2014, 113, No. 095501.
- (31) He, Y.; Shen, Y.; Tang, B.; An, Q. Enhanced Strength and Ductility of Superhard Boron Carbide through Injecting Electrons. J. Eur. Ceram. Soc. 2020, 40, 4428-4435.
- (32) Kresse, G.; Furthmüller, J. Efficient Iterative Schemes for Ab Initio Total-Energy Calculations Using a Plane-Wave Basis Set. Phys. Rev. B 1996, 54, 11169-11186.
- (33) Kresse, G.; Furthmüller, J. Efficiency of Ab-Initio Total Energy Calculations for Metals and Semiconductors Using a Plane-Wave Basis Set. Comput. Mater. Sci. 1996, 6, 15-50.
- (34) Kresse, G.; Hafner, J. Ab initio Molecular Dynamics for Liquid Metals. Phys. Rev. B 1993, 47, 558-561.
- (35) Perdew, J. P.; Burke, K.; Ernzerhof, M. Generalized Gradient Approximation Made Simple. Phys. Rev. Lett. 1996, 77, 3865-3868.
- (36) Blöchl, P. E.; Jepsen, O.; Andersen, O. K. Improved tetrahedron method for brillouin-zone integrations. Phys. Rev. B 1994, 49, 16223-16233.
- (37) Hill, R. The Elastic Behaviour Of a Crystalline Aggregate. Proc. Phys. Soc. A 1952, 65, 349-354.
- (38) Le Page, Y.; Saxe, P. Symmetry-General Least-Squares Extraction of Elastic Data for Strained Materials from Ab Initio Calculations of Stress. Phys. Rev. B 2002, 65, No. 104104.
- (39) Blöchl, P. E. Projector Augmented-Wave Method. Phys. Rev. B **1994**, *50*, 17953-17979.
- (40) Kaduk, B.; Kowalczyk, T.; Van Voorhis, T. Constrained Density Functional Theory. Chem. Rev. 2012, 112, 321-370.
- (41) Kidd, D.; Umar, A. S.; Varga, K. Constrained Density Functional Theory Calculation with Iterative Optimization. Phys. Rev. B 2018, 98, No. 075108.
- (42) Kresse, G.; Joubert, D. From Ultrasoft Pseudopotentials to the Projector Augmented-Wave Method. Phys. Rev. B 1999, 59, 1758-1775.
- (43) Melander, M.; Jónsson, E. Ö.; Mortensen, J. J.; Vegge, T.; García Lastra, J. M. Implementation of Constrained DFT for Computing Charge Transfer Rates within the Projector Augmented Wave Method. J. Chem. Theory Comput. 2016, 12, 5367-5378.
- (44) An, Q.; Goddard, W. A., III Boron Suboxide and Boron Subphosphide Crystals: Hard Ceramics that Shear without Brittle Failure. Chem. Mater. 2015, 27, 2855-2860.
- (45) Roundy, D.; Krenn, C. R.; Cohen, M. L.; Morris, J. W. Ideal Shear Strengths of FCC Aluminum and Copper. Phys. Rev. Lett. 1999, 82, 2713-2716.
- (46) Miles, R. W.; Zoppi, G.; Forbes, I. Inorganic Photovoltaic Cells. *Mater. Today* **2007**, 10, 20–27.

- (47) Altermatt, P. P.; Schenk, A.; Geelhaar, F.; Heiser, G. Reassessment of the Intrinsic Carrier Density in Crystalline Silicon in View of Band-Gap Narrowing. J. Appl. Phys. 2003, 93, 1598-1604.
- (48) Kanevce, A.; Reese, M. O.; Barnes, T.; Jensen, S.; Metzger, W. The Roles of Carrier Concentration and Interface, Bulk, and Grain-Boundary Recombination for 25% Efficient CdTe Solar Cells. J. Appl. Phys. 2017, 121, 214506.
- (49) Deringer, V. L.; Tchougréeff, A. L.; Dronskowski, R. Crystal Orbital Hamilton Population (COHP) Analysis as Projected from Plane-Wave Basis Sets. J. Phys. Chem. A. 2011, 115, 5461-5466.
- (50) Maintz, S.; Deringer, V. L.; Tchougréeff, A. L.; Dronskowski, R. LOBSTER: A Tool to Extract Chemical Bonding from Plane-Wave Based DFT. J. Comput. Chem. 2016, 37, 1030-1035.
- (51) Steinberg, S.; Dronskowski, R. The Crystal Orbital Hamilton Population (COHP) Method as a Tool to Visualize and Analyze Chemical Bonding in Intermetallic Compounds. Crystals 2018, 8, 225.
- (52) Momma, K.; Izumi, F. VESTA 3 for Three-Dimensional Visualization of Crystal, Volumetric and Morphology Data. J. Appl. Crystallogr. 2011, 44, 1272-1276.
- (53) Wade, K. The Structural Significance of the Number of Skeletal Bonding Electron-Pairs in Carboranes, the Higher Boranes and Borane Anions, and Various Transition-Metal Carbonyl Cluster Compounds. J. Chem. Soc. D 1971, 15, 792-793.
- (54) An, Q. Drastic Modification of Lattice Thermal Conductivity in Thermoelectrics Induced by Electron-Hole Pairs. ACS Appl. Mater. Interfaces 2021, 13, 3911-3918.

□ Recommended by ACS

Unveiling the Zero-Phonon Line of the Boron Vacancy **Center by Cavity-Enhanced Emission**

Chenjiang Qian, Jonathan J. Finley, et al.

JUNE 27, 2022 NANO LETTERS

READ C

Defect Engineering of Monoisotopic Hexagonal Boron Nitride Crystals via Neutron Transmutation Doping

Jiahan Li, James H. Edgar, et al.

NOVEMBER 18, 2021

CHEMISTRY OF MATERIALS

READ **C**

Revealing Electron-Phonon Coupling Dependence on the π -Conjugated Groups in Rare-Earth Borates

Fangyan Wang, Yicheng Wu, et al.

FEBRUARY 22, 2022

CRYSTAL GROWTH & DESIGN

READ C

Sc-B₂₄N₂₄: A New Low-Density Allotrope of BN

Xiaoyue Zhang, Xin Cui, et al.

JULY 24, 2022

THE JOURNAL OF PHYSICAL CHEMISTRY C

READ

Get More Suggestions >